

LETTER TO THE EDITOR

Spiral arms and instability within the AFGL 4176 mm1 disk

Katharine G. Johnston¹, Melvin G. Hoare¹, Henrik Beuther², Rolf Kuiper³, Nathaniel Dylan Kee⁴, Hendrik Linz², Paul Boley^{5,6}, Luke T. Maud⁷, John D. Ilee¹, Aida Ahmadi², and Thomas P. Robitaille⁸

¹ School of Physics & Astronomy, E.C. Stoner Building, The University of Leeds, Leeds, LS2 9JT, UK
e-mail: k.g.johnston@leeds.ac.uk

² Max Planck Institute for Astronomy, Königstuhl 17, D-69117 Heidelberg, Germany

³ Institute of Astronomy and Astrophysics, Eberhard Karls University Tübingen, Auf der Morgenstelle 10, D-72076 Tübingen, Germany

⁴ Institute of Astronomy, KU Leuven, Celestijnenlaan 200D, B-3001 Leuven, Belgium

⁵ Moscow Institute of Physics and Technology, 9 Institutskiy per., Dolgoprudny 141701, Russia

⁶ Ural Federal University, 19 Mira st., Ekaterinburg 620075, Russia

⁷ ESO Headquarters, Karl-Schwarzschild-Str. 2, 85748 Garching bei München, Germany

⁸ Aperio Software, Headingley Enterprise and Arts Centre, Bennett Road, Headingley, Leeds, LS6 3HN, UK

Received November 20, 2019

ABSTRACT

We present high-resolution (30 mas or 130 au at 4.2 kpc) Atacama Large Millimeter/submillimeter Array observations at 1.2 mm of the disk around the forming O-type star AFGL 4176 mm1. The disk (AFGL 4176 mm1-main) has a radius of ~ 1000 au and contains significant structure, including a spiral arm on its redshifted side. By fitting the spiral with models of logarithmic and Archimedean spirals, we find that the Archimedean spiral with a varying pitch angle best fits its morphology, suggesting that one or more companions may play a role in creating the spiral structure. As well as signatures of rotation across the disk, we observe gas arcs in CH₃CN connecting to other mm continuum sources in the field, supporting the picture of interactions within a small cluster around AFGL 4176 mm1-main. Using CASSIS LTE modelling of the CH₃CN K-ladder, we determine the temperature and velocity field across the disk, and thus determine a map of the Toomre stability parameter. Our results indicate that the outer disk is gravitationally unstable and already has or is likely to fragment in the future, possibly producing further companions. These observations provide evidence that disk fragmentation is one possible pathway towards explaining the high fraction of multiple systems around high-mass stars.

Key words. Accretion, accretion disks – circumstellar matter – Stars: formation – Stars: massive – Techniques: interferometric

1. Introduction

Recently, ALMA has detected spiral structures in the midplanes of both protostellar (e.g. Tobin et al. 2016; Lee et al. 2019) and protoplanetary disks (e.g. Pérez et al. 2016; Huang et al. 2018; Kurovic et al. 2018) around low-mass ($< 2 M_{\odot}$) stars. In this letter, we present observations which show spiral structure within the disk of the forming massive star AFGL 4176 mm1, which lies at a distance of 4.2 kpc (Green & McClure-Griffiths 2011). This result accompanies recent observations of spiral structure in the disks or inner envelopes around other massive stars (e.g. Csengeri et al. 2018; Maud et al. 2019).

We previously presented ALMA observations of the AFGL 4176 region, uncovering one of the best examples of a near-Keplerian disk around an O-type star (Johnston et al. 2015, hereafter J15). Radiative transfer modelling by J15 of these data determined that the best-fitting disk mass and radius were $12 M_{\odot}$ and 2000 au, respectively, and the inclination was close to face-on ($i = 30^{\circ}$). In Appendix A we show that the best-fitting disk model from J15 is gravitationally unstable in the outer regions of the disk. Thus, we would expect spiral structure to be seen when we observe the disk at higher resolution.

Spiral structure in disks around young high-mass stars has been anticipated by a host of simulations (e.g. Krumholz et al. 2007; Kuiper et al. 2011; Harries et al. 2017; Meyer et al. 2018;

Ahmadi et al. 2019), which predict near-Keplerian disks with spiral arms, sizes on the order of hundreds to thousands of au, and masses of several $\sim 10\%$ of their host stars. In some cases, disk fragments are predicted (e.g. Meyer et al. 2018; Ahmadi et al. 2019; Rosen et al. 2019), which may also have recently been observed for the first time (Ilee et al. 2018).

The spiral structure seen in these simulations stems mainly from their high disk mass, producing disks that are gravitationally unstable. The Toomre parameter Q (Toomre 1964) can be used as a measure of the level of gravitational instability within a disk:

$$Q = \frac{c_s \kappa}{\pi G \Sigma} \quad (1)$$

where c_s is the sound speed, κ is the epicyclic frequency, G is the gravitational constant and Σ is the disk surface density. A range of simulations have shown that values of $Q < 1.5-1.7$ are required for gravitational instability to occur (Durisen et al. 2007, 2008, and references therein).

The importance of gravitational instabilities in high-mass star formation are far-reaching, as they likely play a role in observed variability due to accretion bursts (e.g. Caratti o Garatti et al. 2017; Hunter et al. 2017), as well as having the potential to explain the high binary and multiple fraction for high mass stars (Duchêne & Kraus 2013).

Table 1. ALMA spectral setup.

Central Frequency (GHz)	Bandwidth (GHz)	Number of Channels	Spectral Resolution (kHz)	(km s ⁻¹)
239.298	468.779	1920	282	0.353
241.478	1.875	1920	1129	1.40
253.106	1.875	1920	1129	1.34
255.411	1.875	1920	1129	1.33

Notes. The spectral resolution is given after Hanning smoothing.

2. Observations

We observed AFGL 4176 with the 12 m antenna array of ALMA Cycle 5 under program 2017.1.00700.S (PI: Johnston). The observations were taken in dual polarisation mode in Band 6 at a frequency of ~ 250 GHz (1.2 mm), with one pointing centred on $13^h43^m01.689^s - 62^{\circ}08'51.25''$ (ICRS). The observations were taken in three different configurations on 3 October 2017, 4 November 2017 and 25 November 2017, with baseline lengths ranging between 118.1 m–15.0 km, 113.0 m–13.9 km and 92.1 m–8.5 km, and precipitable water vapours of 1.1, 0.5 and 0.6 mm on each date, respectively. Therefore, the angular resolution for the continuum is ~ 30 mas or ~ 130 au ($d=4.2$ kpc, robust=0.5 weighting) and the largest angular scale that the observations are sensitive to is $\sim 1.6''$ (or 6700 au, corresponding to a baseline of 92.1 m). The number of antennas for each observation was 42, 43 and 44 (with 30, 41 and 43 having useful data, respectively). The primary beam sizes range between 20.5 and 22.0''. The spectral setup is described in Table 1. The bandpass and absolute flux calibrator was J1427-4206, the phase calibrator was J1337-6509, the check source was J1308-6707 and the pointing calibrator was J1424-6807.

The data reduction was carried out using Common Astronomy Software Applications (CASA) version 5.1.1-5 r40000 via the pipeline version 40896 (Pipeline-CASA51-P2-B), and imaging was carried out in CASA version 5.3.0. In addition to the pipeline calibration, we performed phase-only self-calibration to the continuum and applied these solutions to the line data before imaging. The continuum was imaged using multiscale clean and a Briggs weighting parameter of 0.5. The central frequency of the combined continuum image made from the line-free channels is 248.057 GHz (1.21 mm). The line data presented in this letter (K-ladder transitions of CH₃CN) was imaged using multiscale clean, a robust parameter of 1.0 and a channel width of 1 km s⁻¹ to improve sensitivity.

3. Results and Discussion

3.1. 1.2 mm continuum

Figure 1 shows the 1.21 mm continuum emission from the AFGL 4176 region. The new observations show that the source AFGL 4176 mm1 presented in J15 now splits into four sources: mm1-main, mm1b, mm1c and mm1d. The source mm2 is still single and shows an elongation which extends in the direction away from mm1.

Most notably, the new observations show the disk source mm1-main has significant sub-structure. The west side of the disk contains a spiral arm which emanates from the north west of the central region of the disk, whereas the east side resembles an arc-like structure which curves like a closing parenthesis away from the centre of the disk. Meyer et al. (2018) presented simulated ALMA 1.2 mm continuum observations of a radiation-hydrodynamical simulation of a system with similar properties

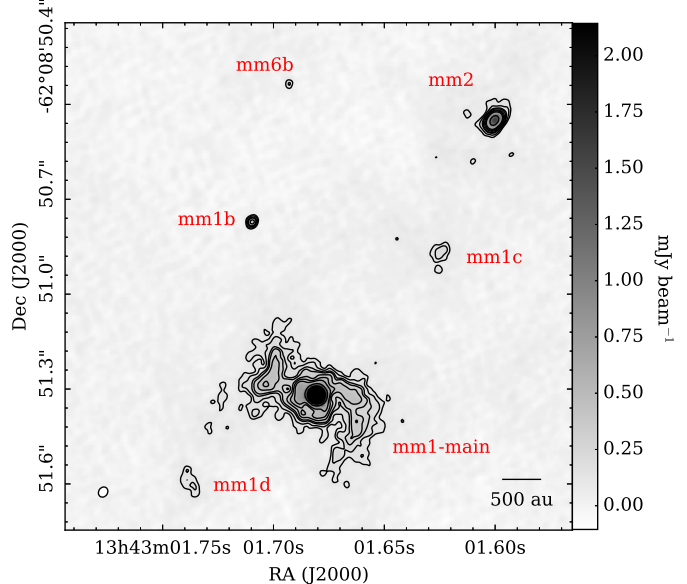


Fig. 1. 1.21 mm continuum emission of the AFGL 4176 region in greyscale and contours ($\sigma = 23 \mu\text{Jy beam}^{-1} \times -5, 5, 7, 10, 12, 16, 20, 25, 50, 100$). The beam is shown in the bottom left corner ($0.034'' \times 0.028'', \text{PA} = -33.5^\circ$), and a scalebar in the right. The mm sources are labelled.

to AFGL 4176 (their Fig. 16). Comparing to our Fig. 1, there are several similarities. If the eastern arc in our observations can be interpreted as another spiral arm which has a fragment forming the southern part of the arc, both disks have two arms, with the morphology in both cases not completely symmetric. In addition, the end of the north eastern spiral arm in the simulated observation resembles the morphology of the eastern arc-like structure, with a peak or possible fragment in the south east end of the arc. Thus, the morphology of the dust in our observations is consistent with simulations of gravitationally unstable disks around forming massive stars.

The peak flux of mm1-main is $10.72 \pm 0.02 \text{ mJy beam}^{-1}$ at a position of $13:43:01.681 - 62:08:51.32$ (ICRS), and the integrated flux above 1σ is $42.67 \pm 0.03 \text{ mJy}$. The integrated flux is slightly smaller than that determined by J15 for mm1 ($50 \pm 4 \text{ mJy}$), but still within 2σ . Therefore, the disk mass is 6.6 M_{\odot} , which should be compared to the mass of $\sim 8 \text{ M}_{\odot}$ determined in J15 using the same assumptions, including $T = 190 \text{ K}$, $\kappa_{\nu} = 0.24 \text{ cm}^2 \text{ g}^{-1}$ and a gas-to-dust ratio of 154. We note however that full radiative-transfer modelling in J15 determined a disk mass of 12 M_{\odot} .

There is a central bright compact source at the centre of the mm1 disk. We fitted and subtracted this central source using imfit in CASA, finding a peak flux of $10.4 \text{ mJy beam}^{-1}$, integrated flux of 13.9 mJy , as well as convolved and deconvolved sizes of $35.6 \times 35.5 \text{ mas}$, $\text{PA} = 55^\circ$ and $21.7 \times 11.6 \text{ mas}$ (corresponding to $91 \times 49 \text{ au}$), $\text{PA} = 56^\circ$, respectively. There is a corresponding compact continuum source at 1.23 cm measured with ATCA with an integrated flux of 1.33 mJy (Johnston et al., submitted). Therefore, the spectral index between the cm and mm compact continuum sources is ~ 0.9 . If the compact sources at both wavelengths are entirely due to ionized gas, then this would indicate there is compact, partially-optically-thick ionized gas associated with the centre of the disk, which may be a jet or a hypercompact HII region. In addition, removal of the compact source from the 1.21 mm emission would reduce the total disk mass from 6.6 to 4.4 M_{\odot} . However, we note that a fraction of the compact mm

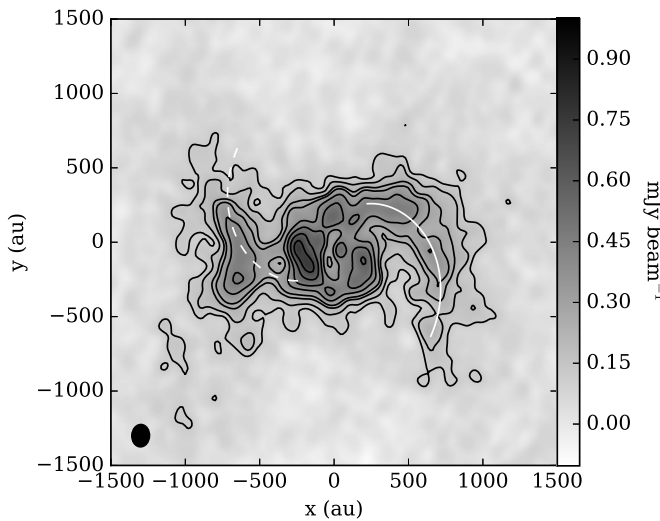


Fig. 2. Deprojected 1.21 mm continuum image of AFGL 4176 mm1-main in greyscale and contours, with the central compact source subtracted (contours: $\sigma = 23 \mu\text{Jy beam}^{-1} \times -5, 5, 7, 10, 12, 16, 20, 25, 30$). The rotated and deprojected beam is shown in the bottom left corner. The best fitting Archimedean spiral (cf. Fig. 3) is plotted as a white line, as well as the same pattern rotated 180° (dashed white line).

source is likely also due to the rising surface density expected at the centre of the disk (as seen in the simulated observation of Meyer et al. 2018).

Using an ellipse with PA=60°, we measure the semi-major axis of mm1-main including the spiral arms at 5σ to be $\sim 0.25''$, giving a disk radius of ~ 1000 au. We also use the ratio of the semi-major-to-minor axes of the disk to determine an estimate of the disk inclination. The smallest semi-minor axis that is consistent with the shape of the disk is 0.15'' (this is illustrated in Figure B.1), providing an upper limit to the inclination of 51°. This is consistent with the inclination of 30° found by the modelling of J15 and with updated modelling in which we find 20° (Johnston et al., in prep.).

In Fig. 2 we show the residual image of mm1-main – with the central compact source removed – deprojected assuming a position angle of 60° and an inclination angle of 20° from our updated modelling (which we assume in the remainder of this analysis). Fig. 3 shows the same data as a function of radius from mm1-main and position angle around the disk. After masking Fig. 3 so that only the western (now right) spiral arm remains, we find the peak radius for each position angle, plotted as a black line on Fig. 3.

Similar to the analysis which was carried out for the DSHARP survey (e.g. Kurtovic et al. 2018; Huang et al. 2018), we fit the peak positions of the western spiral arm with both logarithmic and Archimedean spirals. The equations for the models, as a function of radius r and position angle θ around the disk, and best fit parameters are given in Table 2. To calculate the χ^2 values, we assume an error in determining the peak position in radius is half the beam size divided by 5 (the lowest signal-to-noise in the arm). We also weight each datapoint by the spacing in beams between the sampled position angles at each radius to account for correlation within the scale of a beam. With a lower χ^2 of 6.2, the Archimedean spiral model more-closely reproduces the data. Since the likelihood of each model being correct is proportional to $\exp(-\chi^2/2)$, the relative probability of the Archimedean model being the correct representation of the data is $>99.8\%$.

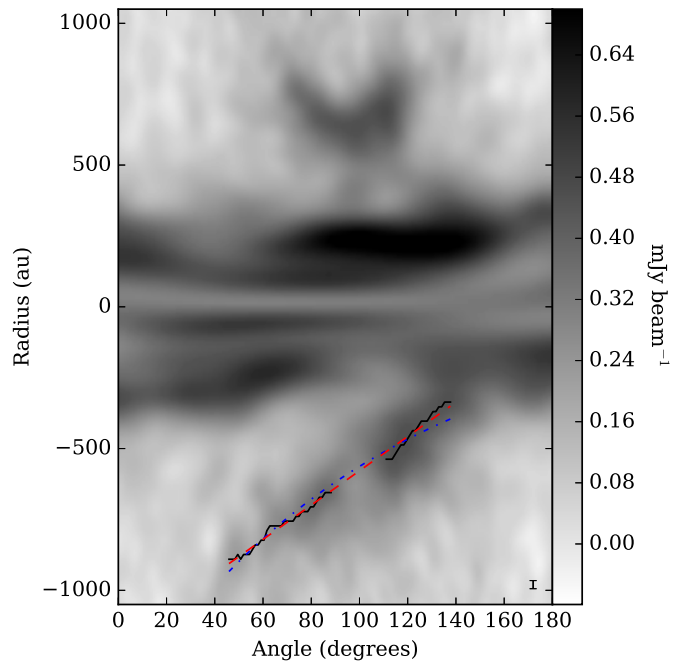


Fig. 3. Flux density as a function of radius and position angle. The peak radius for each position angle is plotted as a black line for the western spiral arm, and the blue dot-dashed and red dashed lines show the best fits for logarithmic and Archimedean spiral models, respectively. A positional error bar is shown in the bottom right corner.

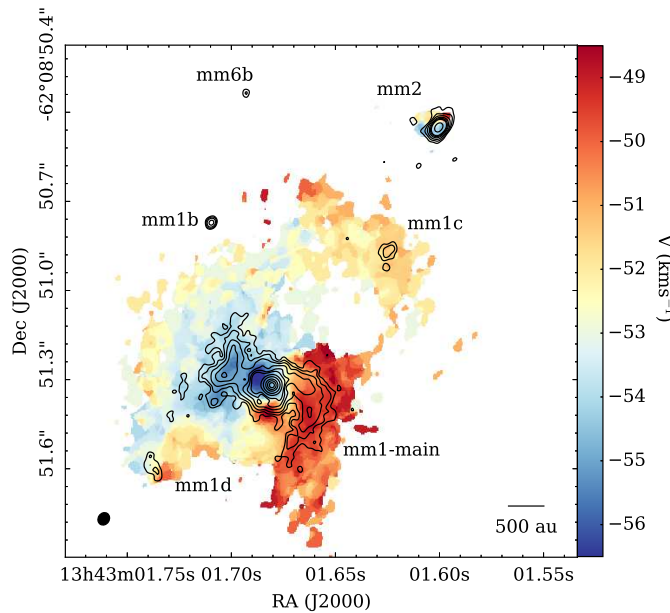
Symmetric, tightly-wound logarithmic spirals with a constant pitch angle are expected from simulations of gravitational instabilities in disks (e.g. Cossins et al. 2009), whereas asymmetric, Archimedean spirals with a varying pitch angle are expected in the case where a companion induces spiral arms (e.g. Rafikov 2002; Forgan et al. 2018). Therefore, although the analysis in Appendix A would indicate the outer regions of the disk are Toomre unstable, the morphology of the western spiral, and the fact there is not a clear symmetrical spiral pattern on the other side of the disk, suggests that the spiral structure is generated to some degree by the existence of one or more nearby companions. In fact, the other continuum sources in the field seen in Fig. 1 may act as these, and they themselves may have been produced by previous episodes of gravitational instability within the disk and later ejected, or formed from the surrounding cloud.

3.2. CH_3CN line emission

Figure 4 presents the first moment map of the CH_3CN J=13-12 K=3 line emission from AFGL 4176, overlaid with contours of 1.21 mm continuum emission. The velocity gradient across the disk which was originally seen by J15 is apparent in the data. However, further details can now also be seen, such as a velocity gradient across the inner part of the redshifted spiral arm. On the larger scales, there is evidence of a gas or tidal link between mm1-main and mm1c, which extends in a north-west direction from the blueshifted side of the disk. The direction of this arm mirrors the redshifted spiral on the west of the disk. Therefore, the gas emission from the AFGL 4176 region shows tentative evidence of tidal interactions between mm1-main and possible companions such as mm1c, which may be exciting spiral arms within mm1-main. An alternative explanation is that the process of ejection of mm1c from the disk could produce a stretched

Table 2. Spiral models and associated fit parameters

Spiral type	Equation	r_0	b	pitch angle	χ^2
Logarithmic	$r = r_0 \exp(b\theta)$	-3325 ± 209 au	-0.5356 ± 0.0225	$\arctan(1/b) = -61.8^\circ$	19.3
Archimedean	$r = r_0 + b\theta$	-1728 ± 38 au	346.7 ± 12.5 au	$b/r = -22.3 \rightarrow -59.1^\circ$	6.2

**Fig. 4.** CH_3CN $J=13-12$ $K=3$ first moment map in colourscale and 1.21 mm continuum in contours (same as in Fig. 1). The beam is shown in the bottom left corner ($0.043'' \times 0.038''$, PA= -32.6°), and a scalebar in the right.

gas link between the secondary fragment or protostar and the primary.

Similar to the analysis carried out by J15, we determine excitation temperature, velocity, linewidth, and column density maps across AFGL 4176 by fitting the CH_3CN and $\text{CH}_3^{13}\text{CN}$ $J=13-12$ K-ladder emission associated with each pixel with the spectrum analysis tool CASSIS¹. Using the same algorithm and setup as described in J15 but with slightly updated initial parameter ranges ($T_{\text{ex}} = 50 - 350$ K, $v_{\text{LSR}} = -58 - -48$ km s $^{-1}$, $v_{\text{FWHM}} = 0.5 - 15$ km s $^{-1}$ and $N_{\text{mol}} = 1 \times 10^{15} - 1 \times 10^{18}$ cm $^{-2}$), we determine the excitation temperature T_{ex} and velocity across the disk, shown in Figure 5. As we assume LTE in our analysis, T_{ex} therefore provides an estimate of the kinetic temperature. Maps of the remaining parameters (linewidth and column density) are presented in Appendix C as Figs. C.1 and C.2. The maps in Figure 5 are de-projected and are clipped to the 4σ level in the continuum maps (shown as contours).

Figure 5a shows that the temperature is lower towards the arc of continuum emission on the left, but higher in the inner leading section of the western spiral arm on the right, and directly to the upper left of the central source. We note that increased temperatures within spiral arms are seen in many simulations of self-gravitating disks (e.g. Boley & Durisen 2008). Figure 5b shows the velocity gradient across the entire disk, as well as a velocity gradient across the inner part of the disk within several hundred au.

3.3. Resolved Toomre Q map

We use the results from previous sections to construct a map of the Toomre parameter Q across the disk, as given in equation 1, similar to the analyses conducted by Ahmadi et al. (2018) and Maud et al. (2019). The sound speed c_s can be calculated from the temperature, using the equation

$$c_s = \sqrt{\frac{kT}{2.8m_p}}, \quad (2)$$

where k is the Boltzmann constant, T is the temperature found from CASSIS and m_p is the mass of a proton. The angular velocity Ω was found by subtracting the systematic velocity ($v_{\text{lsr}} = -52.5$ km s $^{-1}$) from the velocity map determined by CASSIS, de-projecting the velocities by $\sin i$ and then dividing by the radius r at each point in the disk to convert from tangential to angular velocities. Here we assume that the disk is close to Keplerian so that $\kappa = \Omega$. Finally, the surface density Σ can be calculated using the equation

$$\Sigma = \frac{gS_{\text{peak}}}{\Theta B(\nu, T)\kappa_\nu} \quad (3)$$

where g is the gas-to-dust ratio (154, Draine 2011), S_{peak} is the peak flux of the ALMA continuum with the central compact source removed, Θ is the ALMA continuum beam area, $B(\nu, T)$ is the black body function and κ_ν is the opacity (0.24 cm 2 g $^{-1}$ at 1.21 mm for $R_V = 5.5$, Draine 2003a,b).

Figure 6 shows the resulting map of Q across the disk. The purple areas in the map show parts of the disk which are Toomre unstable ($Q < 1.5 - 1.7$, Durisen et al. 2007). There is an artefact of low Q in the centre of the disk caused by the velocity quickly shifting from blue to redshifted. However, further out in the disk we can see that the left (eastern) arc is clearly Toomre unstable, which may already contain a fragment at its lower end, as well as the densest parts of the western spiral on the right. Thus, our analysis shows that this disk has the right conditions to undergo fragmentation that may produce further companions.

We note that the CH_3CN does not trace the midplane, but hotter material higher in the disk atmosphere, and although the disk is not globally optically thick, it may be locally, increasing the surface density in the densest parts of the disk. These optically thick parts of the disk would have to be unresolved, as the < 1 mJy beam $^{-1}$ emission from the outer disk has a brightness temperature of < 20 K. Hence by comparison with Fig. 5a the outer disk is not optically thick at our resolution. From equations 1, 2 and 3 we can see that lowering the temperature and raising the surface density act to lower Q . Therefore, in this case, our analysis provides an upper limit to Q and thus a lower limit to the level of instability of the disk.

In the case the dust opacity is up to a factor of two higher, as our radiative transfer modelling suggests may be the case, this would mean that only parts of the disk in Fig. 6 with $Q < 0.75 - 0.85$ would be unstable, which still occurs in the left (eastern) side of the disk.

¹ CASSIS is developed by IRAP-UPS/CNRS (<http://cassis.irap.omp.eu>).

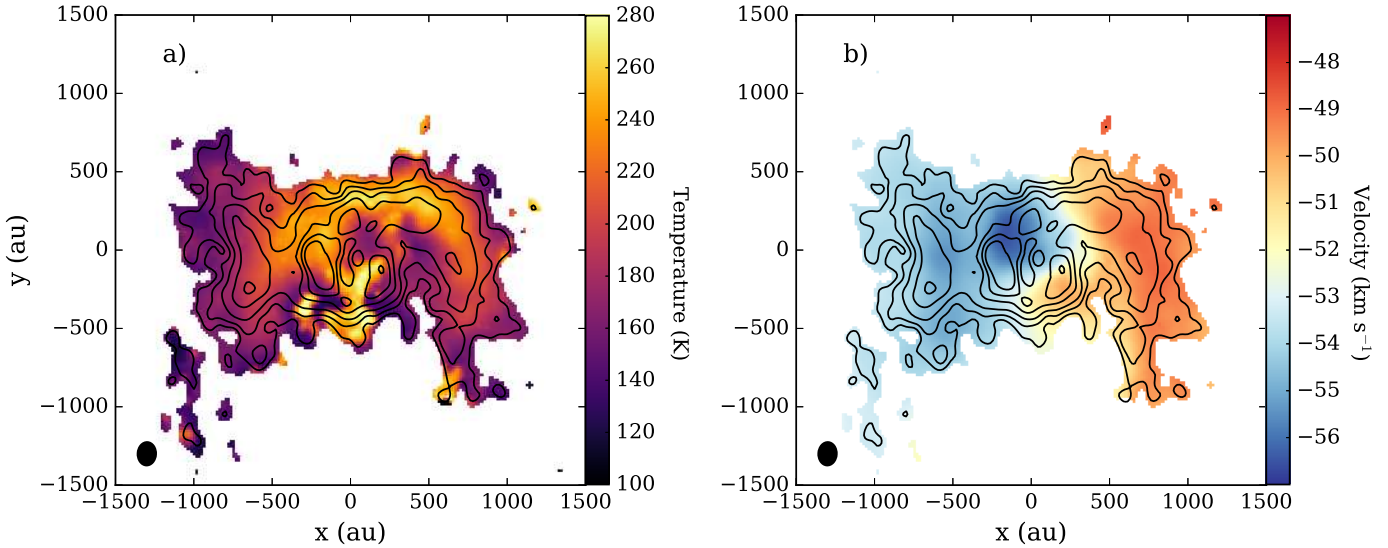


Fig. 5. Results of CASSIS modelling. Panel a) shows the excitation temperature, and panel b) shows the observed velocity. Both maps have been deprojected similarly to Fig. 2 (note that the velocities are not yet corrected for inclination). The 1.21 mm continuum emission as shown in Fig. 2 is overplotted as contours in both panels. The maps are masked to values above 4σ in the continuum map. The deprojected beam is shown in the bottom left corner of each panel.

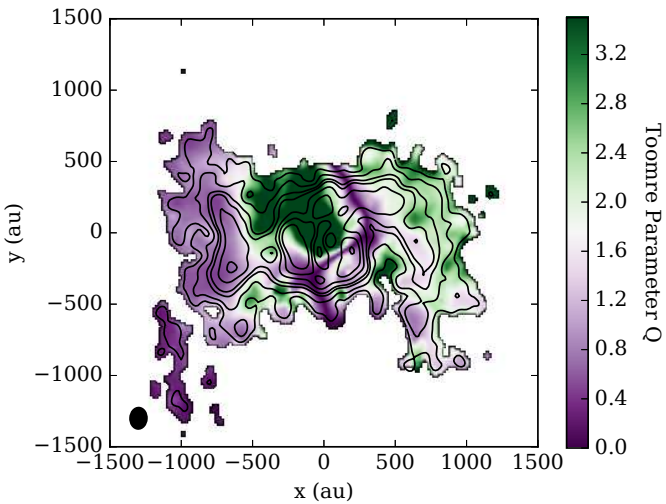


Fig. 6. Deprojected map of Q , similar to that shown for Fig. 5.

4. Conclusions

We present high-resolution (~ 30 mas) 1.2 mm ALMA observations of the AFGL 4176 disk. We find that the disk is ~ 1000 au in radius and contains a spiral arm which is best fit by an Archimedean spiral, suggesting companions may have played a role in producing the disk structure. The CH_3CN gas emission shows evidence for gas arcs which link AFGL 4176 mm1-main to other mm sources in the field, thus providing more evidence of tidal interactions. We produce a map of the Toomre parameter across the disk and find that the disk and spiral arms have already or are likely to fragment in future, possibly forming companions, showing that both current companions and gravitational instabilities play a combined role in creating structure in the AFGL 4176 mm1-main disk. These results have important implications for understanding the origin of the high fraction of multiple systems observed for high-mass stars.

Acknowledgements. JDI acknowledges support from STFC under ST/R000549/1. AA and HB acknowledge support from the European Research Council under the Horizon 2020 framework programme via the ERC Consolidator Grant CSF-648505. H.B. further acknowledges support from the Deutsche Forschungsgemeinschaft in the Collaborative Research Center (SFB 881) “The Milky Way System” (subproject B1). RK acknowledges financial support via the Emmy Noether Research Group on Accretion Flows and Feedback in Realistic Models of Massive Star Formation funded by the German Research Foundation (DFG) under grant no. KU 2849/3-1 and KU 2849/3-2.

References

- Ahmadi, A., Beuther, H., Mottram, J. C., et al. 2018, *A&A*, 618, A46
- Ahmadi, A., Kuiper, R., & Beuther, H. 2019, arXiv e-prints, arXiv:1909.04051
- Boley, A. C. & Durisen, R. H. 2008, *ApJ*, 685, 1193
- Caratti o Garatti, A., Stecklum, B., Garcia Lopez, R., et al. 2017, *Nature Physics*, 13, 276
- Cossins, P., Lodato, G., & Clarke, C. J. 2009, *MNRAS*, 393, 1157
- Csengeri, T., Bontemps, S., Wyrowski, F., et al. 2018, *A&A*, 617, A89
- Draine, B. T. 2003a, *ARA&A*, 41, 241
- Draine, B. T. 2003b, *ApJ*, 598, 1017
- Draine, B. T. 2011, *Physics of the Interstellar and Intergalactic Medium*
- Duchêne, G. & Kraus, A. 2013, *ARA&A*, 51, 269
- Durisen, R. H., Boss, A. P., Mayer, L., et al. 2007, *Protostars and Planets V*, 607
- Durisen, R. H., Hartquist, T. W., & Pickett, M. K. 2008, *Ap&SS*, 317, 3
- Forgan, D. H., Ille, J. D., & Meru, F. 2018, *ApJ*, 860, L5
- Green, J. A. & McClure-Griffiths, N. M. 2011, *MNRAS*, 417, 2500
- Harries, T. J., Douglas, T. A., & Ali, A. 2017, *MNRAS*, 471, 4111
- Huang, J., Andrews, S. M., Pérez, L. M., et al. 2018, *ApJ*, 869, L43
- Hunter, T. R., Brogan, C. L., MacLeod, G., et al. 2017, *ApJ*, 837, L29
- Ille, J. D., Cyganowski, C. J., Brogan, C. L., et al. 2018, *ApJ*, 869, L24
- Johnston, K. G., Robitaille, T. P., Beuther, H., et al. 2015, *ApJ*, 813, L19
- Kratter, K. & Lodato, G. 2016, *ARA&A*, 54, 271
- Krumholz, M. R., Klein, R. I., & McKee, C. F. 2007, *ApJ*, 665, 478
- Kuiper, R., Klahr, H., Beuther, H., & Henning, T. 2011, *ApJ*, 732, 20
- Kurtovic, N. T., Pérez, L. M., Benisty, M., et al. 2018, *ApJ*, 869, L44
- Lee, C.-F., Li, Z.-Y., & Turner, N. J. 2019, *Nature Astronomy*, 466
- Maud, L. T., Cesaroni, R., Kumar, M. S. N., et al. 2019, *A&A*, 627, L6
- Meyer, D. M.-A., Kuiper, R., Kley, W., Johnston, K. G., & Vorobyov, E. 2018, *MNRAS*, 473, 3615
- Pérez, L. M., Carpenter, J. M., Andrews, S. M., et al. 2016, *Science*, 353, 1519
- Rafikov, R. R. 2002, *ApJ*, 569, 997
- Rosen, A. L., Li, P. S., Zhang, Q., & Burkhardt, B. 2019, arXiv e-prints, arXiv:1902.10153
- Tobin, J. J., Kratter, K. M., Persson, M. V., et al. 2016, *Nature*, 538, 483
- Toomre, A. 1964, *ApJ*, 139, 1217

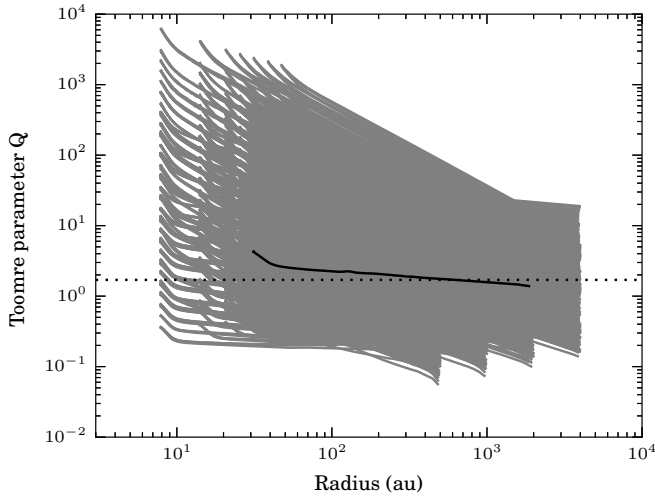


Fig. A.1. Toomre parameter Q in the disk midplane as a function of radius for all of the models in the grid presented in J15, shown as grey lines. The best fit is shown as a black line. The dotted horizontal line is at a value of $Q=1.7$.

Appendix A: Disk stability from axisymmetric modelling

Figure A.1 presents the Toomre parameter Q calculated as a function of radius for all of the models in the grid that was described in J15. The best-fitting model is shown as a black line. As well as including a centrally-condensed envelope, the density structure of each model contained a hydrostatically-flared disk in Keplerian rotation (defined in this case so that the disk velocity takes into account the mass within a given radius). As part of the modelling, the temperature throughout the disk was also calculated for each model using the Monte-Carlo radiative transfer code *Hyperion*, as detailed in J15. Therefore, knowing the disk density, velocity and temperature allows the Toomre parameter as a function of radius in the disk to be calculated. Fig. A.1 shows that the value of Q in the midplane of the best-fitting model reaches below a value of 1.7, shown as a dotted line, in the outer regions of the disk (>620 au). Hence, we would expect the outer regions of the disk around AFGL 4176 mm1 to be unstable, possibly containing spiral arms and fragments. This is also supported by the fact that the disk mass was found to be $12 M_{\odot}$, which is almost half that of the central star ($25 M_{\odot}$), and systems with high disk-to-star mass ratios ($\gtrsim 0.1$) are expected to have gravitationally unstable disks (Kratter & Lodato 2016).

Appendix B: Measuring the geometry of the mm1-main disk from continuum emission

Figure B.1 shows a zoom-in of the 1.21 mm continuum emission from mm1-main with ellipses used to measure its inclination over plotted (cf Section 3.1). The red ellipse shows the smallest reasonable semi-minor axis of $0.15''$, which corresponds to $i = 51^\circ$, whereas the blue dashed ellipse shows the geometry expected for $i = 20^\circ$ (the best fitting inclination from our updated modelling).

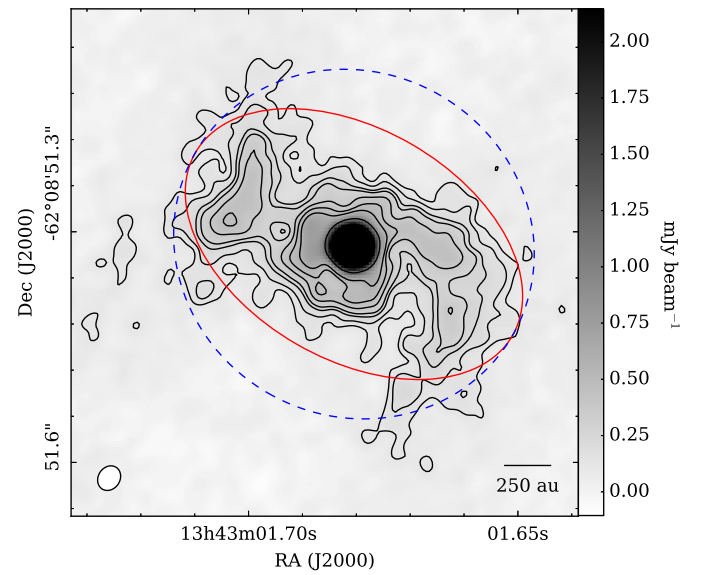


Fig. B.1. 1.21 mm continuum emission of AFGL 4176 mm1-main in greyscale and contours ($\sigma = 23 \mu\text{Jy beam}^{-1} \times -5, 5, 7, 10, 12, 16, 20, 25, 50, 100$). The beam is shown in the bottom left corner ($0.034'' \times 0.028''$, $\text{PA} = -33.5^\circ$), and a scalebar in the right. Two ellipses with semi-major axes of 1000 au or $\sim 0.24''$ are shown, one with a semi-minor axis of $0.15''$ (solid red, corresponding to $i = 51^\circ$) and the other with a semi-minor axis of $0.22''$ (dashed blue, corresponding to $i = 20^\circ$).

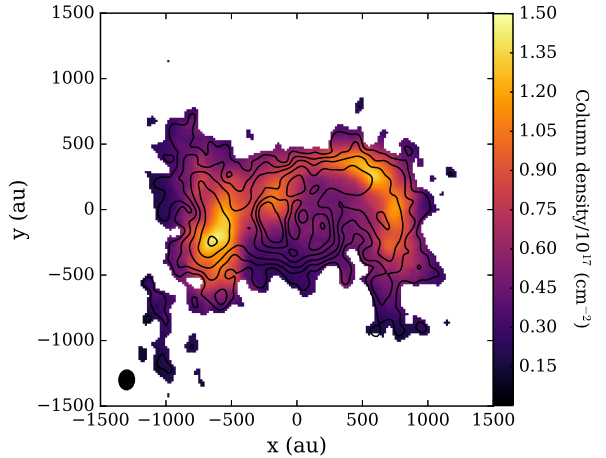


Fig. C.1. Results of CASSIS LTE modelling similar to Fig. 5 but for column density.

Appendix C: Maps of column density and linewidth from CASSIS modelling

Figure C.1 (column density) and Figure C.2 (linewidth) show the remaining maps resulting from the CASSIS LTE modelling. The column density shown in Fig. C.1 is highest in the leading section of the right or western spiral arm, offset from the spiral peak seen in the continuum, as well as in the lower end of the left or eastern arc, towards the continuum peak within the arc. The linewidth shown in Fig. C.2 shows a ring of high values around the position of the subtracted continuum source, which is highest to the lower right.

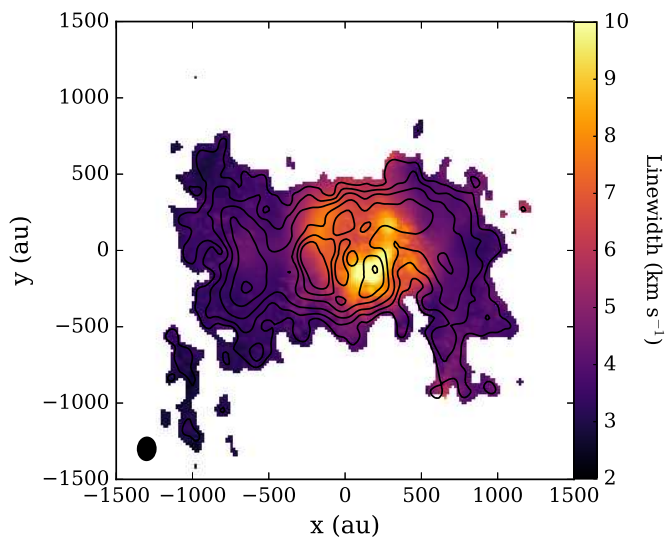


Fig. C.2. Results of CASSIS LTE modelling similar to Fig. 5 but for linewidth.